Axial Descent of Variable-Pitch Multirotor Configurations: An Experimental and Computational Study for Mars Deployment Applications

Marcel Veismann
Graduate Student
California Inst. of Tech.
Pasadena, CA, USA

Skylar Wei
Graduate Student
California Inst. of Tech.
Pasadena, CA, USA

Sarah Conley
Aerospace Eng.
NASA Ames Research Center
Moffett Field, CA, USA

Larry Young
Aerospace Eng.
NASA Ames Research Center
Moffett Field, CA, USA

Jeff Delaune
Robotics Technologist
NASA JPL, California Inst. of Tech.
Pasadena, CA, USA

Joel Burdick
Prof. of Mech. & Bioengineering
California Inst. of Tech.
Pasadena, CA, USA

Morteza Gharib
Prof. of Aero. & Bioinspired Eng.
California Inst. of Tech.
Pasadena, CA, USA

Jacob Izraelevitz
Robotics Technologist
NASA JPL, California Inst. of Tech.
Pasadena, CA, USA

ABSTRACT

For future helicopter-only Mars missions, NASA-JPL has proposed a novel entry, descent, and landing technique, in which the rotorcraft is deployed from the aeroshell in mid-air before landing. However, this approach is likely to subject the rotorcraft to unfavorable vortex ring state aerodynamics during deployment. To address this, the performance of a variable-pitch multirotor in axial descent was investigated using two parallel approaches: an experimental free-flight wind tunnel campaign and analogous computational efforts utilizing the tool RotCFD. Results indicated significant mean thrust losses of up to 20% compared to hover conditions, as well as heavily amplified rotor thrust fluctuations and vehicle attitude oscillations with increasing descent rate. Meanwhile, discrepancies between computations and experiments were observed, primarily regarding the descent rates where maximum thrust losses occur. Additional studies performed within the computational environment indicated that the vehicle fuselage and rotor-rotor interactions have significant impacts on the rotor performance in descent.

NOTATION

A	Rotor Disk Area	m^2
c	Blade Chord Length	m
C_l	Sectional Lift Coefficient	—
C_{l_α}	Lift-Curve Slope	—
C_T	Thrust Coefficient	—
B	Tip Loss Correction Factor	—
f_s	Sampling Rate	$1/\text{s}$
g	Gravitational Acceleration	m/s^2
m	Vehicle Mass	kg
Ma	Mach Number	—
N_b	Rotor Blade Count	—
PWM	Pulse Width Modulation Length	s
r	Radial Distance Fraction	—
r_c	Rotor Root Cutout	—
R	Rotor Radius	m
Re	Reynolds Number	—
T	Thrust	N
v_i	Induced Velocity	m/s
v_h	Induced Velocity in Hover	m/s
v'_x, v'_y	Horizontal Vehicle Velocities (Lab Frame)	m/s
v_z	Net Simulated Descent Velocity	m/s
v'_z	Vertical Vehicle Velocity (Lab Frame)	m/s
$\ddot{z}_b$	Vertical Acceleration (Body Frame)	m/s^2
α	Blade Section Angle of Attack	rad
α_0	Zero-Lift Angle of Attack	rad
Θ	Vehicle Pitch Angle	rad
θ	Blade Pitch Angle	rad
$\theta_{.75}$	Blade Pitch at 75% Radius	rad
κ	Empirical Inflow Factor	—
λ	Inflow Ratio	—
μ	Advance Ratio	—
ρ	Density	kg/m^3

σ	Rotor Solidity	–
Φ	Vehicle Roll Angle	rad
ϕ	Relative Inflow Angle	rad
Ψ	Vehicle Yaw Angle	rad
Ω	Rotor Angular Frequency	rad/s

INTRODUCTION

The Ingenuity Mars Helicopter (Refs. 1,2), accompanying the Mars 2020 rover mission, is projected to demonstrate the first powered flight on another planet, opening up new approaches of extraterrestrial exploration. While this mission is still ongoing, research is already underway to prepare a potential helicopter-only science mission. This mission anticipates a dedicated science rotorcraft, significantly larger than the current Ingenuity system, to support the increased weight of an additional science payload. One concept, the Mars Highland Helicopter (MHH) (Ref. 3), leverages the design heritage of the Ingenuity system, by adopting a similar, counter-rotating, co-axial rotor arrangement. More recent developments also consider multirotor platforms instead of a co-axial rotorcraft for the design of the second generation of Mars helicopter (Ref. 4). All of the future Mars helicopter concepts use large rotors ($R > 0.6\,\mathrm{m}$) in order to sustain flight on Mars, and it is likely that they will utilize variable-pitch control, also known as variable collective or collective control due to control bandwidth considerations. Traditionally, terrestrial hobby multirotor vehicles employ fixed-pitch, variable-RPM control, which is mechanically simple and robust; however, there is a fundamental limit as rotor size increases, beyond which fixed-pitch system are no longer able to overcome the large moment of inertia for quick RPM adjustments (Ref. 5) and safely controlling the rotor performance by varying RPM alone becomes infeasible.

Aside from apparent advantages over rover-type explorers regarding traversing rough terrain and covering larger surface areas, a helicopter-only mission offers novel alternatives to the traditional atmospheric entry, descent, and landing (EDL) procedure. Up to date, Mars surface missions have all landed via dedicated landing systems such as high-G airbags or rocket thrusters, which typically require 100+ kg (220 lb) of specialized hardware to decelerate from $\sim$30 m/s (98 ft/s) parachute terminal velocity to almost 0 m/s before touch-down. Since a helicopter can readily slow itself down over this velocity range, these traditional landing systems could be omitted entirely in future helicopter-only missions if the rotorcraft is instead deployed in mid-air from the entry capsule at the end of the parachute phase. Initial Mid-Air Deployment (MAD) concepts propose the following sequence: lowering of the rotorcraft from the stowed configuration inside the aeroshell after heatshield separation, rotor spool up, and subsequent separation from the entry capsule backshell before transitioning to stable controlled flight. The Dragonfly mobile lander designed for Titan (Ref. 6) plans to use a similar sequence, although much slower timeline. The Mars-MAD sequence is visualized in Fig. 1. By not relying on dedicated landing hardware, MAD offers the potential to drastically reduce the total mission mass and cost. Furthermore, low-mass entry vehicles on Mars decelerate at higher altitudes, enabling missions to the Martian highlands currently deemed unreachable by traditional Mars entry systems. These highlands are the oldest terrains on Mars, accounting for 50% of the surface, have never been explored. They could solve outstanding questions in planetary science today related to the operation of the Mars dynamo, the formation of the early crust, and the evolution of the early environments (Ref. 7). For more motivation of the MAD concept as well as the deployment and descent details, readers can refer to prior publications (Refs. 3, 8).

One of the most pressing engineering challenges associated with MAD is the fact that the entry configuration is descending at parachute velocity during deployment, and the rotorcraft will therefore experience axial (and possibly non-axial) flight conditions, potentially subjecting it to adverse descent aerodynamics, generally referred to as vortex ring state (VRS) (Ref. 9). These aerodynamic disturbances typically arise when a rotorcraft descends into its own wake, introducing significant unsteadiness in the rotor loads, leading to severe lift losses and reduced control authority. The deployment is further complicated by the presence of the entry capsule backshell, which presents a risk of vehicle damage in the event of recontact and has to be avoided at all costs during rotorcraft separation. In addition, the convex geometry of the backshell increases the complexity of the local flow field around the rotorcraft in the initial stages of deployment.

Consequently, the MAD project currently utilizes Earth-analog experiments and computational efforts to assess the feasibility of deploying a rotorcraft in mid-air and outline the most promising deployment strategies. Of key interest are a comprehensive evaluation of rotor aerodynamics and vehicle dynamics during deployment. A scaled backshell was also constructed to specifically study rotorcraft-backshell flow interactions but this is still on-going work. This paper presents work conducted in this context, investigating the post-release, free-flight, vertical-descent phase of the MAD flight envelope, without considering the backshell aerodynamics. In particular, the thrust loss and thrust fluctuation experienced by variable-pitch multirotor craft in axial descent was quantified.

Previously, considerable research efforts have been dedicated to investigating the effect of the VRS aerodynamics on the rotor performance, universally observing losses in the mean rotor thrust combined with significant increasing thrust fluctuations. However, previous studies have been largely limited to large-scale, single-rotor helicopters. More recent efforts have also started examining the performance of small-scale, low Reynolds number rotors in the VRS with fixed pitch (Refs. 10, 11) as well as variable pitch (Refs. 12, 13), but these studies are, similarly, limited to single rotors only. Therefore, this work seeks to fill this knowledge gap for low Reynolds number, variable-pitch multirotor platforms. Of further interest was how variations in the rotor pitch angle affect the overall rotor performance in the VRS and to understand the degree of agreement of simulations tools.

The experimental campaign consisted of free-flight experi-
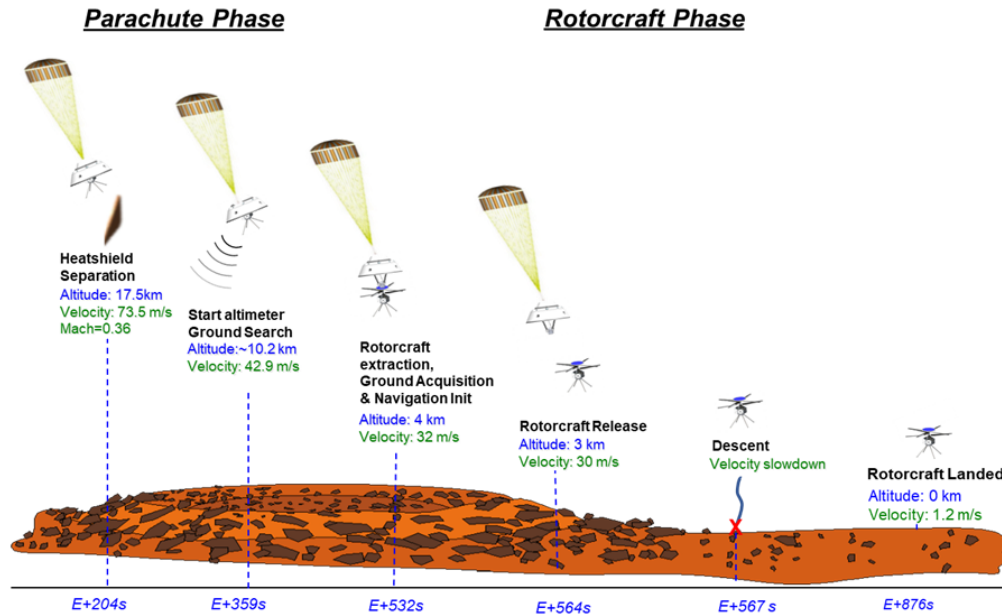
Figure 1. Proposed EDL-sequence of a Mars science rotorcraft with Mid-Air Deployment: the helicopter is lowered from the backshell at the end of the parachute phase, rotors are spun up, the rotorcraft is released and transitions to a controlled flight for landing. Reproduced from (Ref. 8).

ments of a variable-pitch quadrotor in a vertical wind tunnel to simulate axial descent scenarios (see Figs. 5 and 15 for illustration). Without rigid connections to a load cell, nominal in-flight forces were predicted using rotor pitch commands sent by the vehicle flight controller. This estimated thrust could be compared against the instantaneous thrust generated by the vehicle in descent based on acceleration measurements to quantify the thrust loss as a function of descent rate. Thus, in-flight forces could be quantified without relying on a rigid mounting and without restricting vehicle dynamics, to obtain new insights into the true axial descent characteristics of a variable-pitch multirotor. Parallel to the experiments, mid-fidelity computational fluid dynamics simulations were performed using the tool RotCFD (Ref. 14) for a wide range of rotor pitch angles (5° - 15°) and descent rates (0 m/s - 6 m/s). To facilitate comparisons between simulations and the experimental results, a near-identical rotor and fuselage geometry as well as identical operational parameters were used. The computational environment, furthermore, allowed to perform a comparison study involving a single rotor and four rotors without fuselage to assess rotor-rotor interactions and effects of the vehicle fuselage on the overall descent performance. All experimental and computational efforts throughout the study were performed under Earth relevant atmospheric conditions, but scaling considerations of rotor parameters to the Ingenuity system and the proposed MHH are presented to assess the research's applicability for future Mars scenarios. The goal of this study is to use the experiments for validation of the analogous computational analysis, which can ultimately be performed for Martian conditions. Meanwhile, research presented in this paper also has direct applicability for any terrestrial variable-pitch multirotor vehicle in axial de-

scent. This will become increasingly relevant when multirotor systems are scaled up to a point (e.g. for cargo transportation), where a traditional fixed-pitch, variable-RPM control is no longer feasible.

ROTOR AERODYNAMICS REVIEW

The following section briefly reviews relevant rotorcraft aerodynamics including variable-pitch rotor thrust models and vortex ring state aerodynamics. This review is not meant to be comprehensive and readers are encouraged to refer to the cited literature for further reading.

Variable-Pitch Rotor Thrust in Hover

Variable collective pitch control employed on a rotor allows control of the thrust output by means of changing the local angle of attack of the rotor blade elements via a swashplate mechanism, while the rotor spins at a constant rate. Helicopters typically combine collective pitch control with cyclic pitch control to change the helicopter's direction of movement. In the case of a variable-pitch multirotor, each rotor features independent pitch control to regulate attitude and direction of movement through differential rotor thrust, thus not needing cyclic control. Meanwhile, the total vehicle thrust output is the sum of the thrust of each individual rotor.

Using the blade element theory, the individual rotor thrust can be estimated from operational parameters based on the radial distribution of aerodynamic loading of the rotor blade. The following analysis briefly summarizes analytic blade element theory rotor thrust models suggested by (Refs. 15, 16) and assumes untwisted blades with symmetric airfoils ($\alpha_0 = 0$),

3

which is representative of the rotor geometry utilized throughout the study. The effective angle of attack of a blade element is defined as difference between the geometric pitch angle, θ, and the relative inflow angle, ϕ:

$$\alpha = \theta - \phi, \tag{1}$$

and the local blade lift coefficients is given by

$$C_l = C_{L_\alpha}(\alpha - \alpha_0) = C_{L_\alpha}(\theta - \phi - \alpha_0). \tag{2}$$

According to the local blade element theory, the local rotor thrust increment of a blade element can be modeled as:

$$dC_T = \frac{1}{2}\left(\frac{N_b}{\pi R}\right)c(r)C_l r^2 \, dr, \tag{3}$$

where r is the radial distance fraction. The total thrust coefficient is the incremental thrust integrated along the blade:

$$C_T = \frac{1}{2}\left(\frac{N_b}{\pi R}\right)\int_0^1 c(r)C_l r^2 \, dr \tag{4}$$

with $C_T = T/\rho A(\Omega R)^2$. To evaluate C_T generally requires information regarding spanwise variations of the lift coefficient, $C_l = C_l(\alpha, Re, Ma)$ as well as the inflow, $\lambda = (v_i + v_z)/(\Omega R)$, determining the relative inflow angle, which can typically not be solved analytically. However, by making the assumption of a constant lift-curve-slope, C_{l_α}, and uniform inflow velocity along the span

$$C_{L_\alpha} \approx 2\pi = const. \tag{5}$$
$$\lambda = \phi r = const. \tag{6}$$

yields the expression

$$C_T = \frac{1}{2}\left(\frac{N_b}{\pi R}\right)C_{L_\alpha}\int_0^1 c(r)\left(\theta r^2 - \lambda r\right) dr \tag{7}$$

and for hover, $\lambda_h = \sqrt{C_T/2}$. Furthermore, to account for non-ideal flow conditions, the tip loss factor B can be introduced, which is treated as a reduction in the effective blade radius, with B usually between 0.95 and 0.98 for full-scale helicopters. However, on low aspect ratio rotors B can be considerably lower. Previously, various methods for calculating the tip loss factor based on the rotor loading or geometry have been suggested (Ref. [16]):

$$B = 1 - \frac{\sqrt{2C_T}}{N_b} \tag{8a}$$

$$B = 1 - \frac{c(r=1)}{2R} \tag{8b}$$

$$B = 1 - \frac{2c(r=0.7)}{3R} \tag{8c}$$

resulting in a wide range of values of approximately $0.88 < B < 0.94$ for the given rotor geometry and thrust coefficients found in this study. Incorporating the tip loss factor, Eqn. 11 becomes

$$C_T = \frac{1}{2}\left(\frac{N_b}{\pi R}\right)C_{L_\alpha}\int_{r_c}^B c(r)\left(\theta r^2 - \sqrt{\frac{C_T}{2}}r\right) dr, \tag{9}$$

which can be solved numerically and iteratively for C_T for a set of given geometric and operational rotor parameters (R, $c(r)$, N_b, θ, r_c, Ω). For the case of rectangular rotor blades ($c = const.$) and insignificant root cutout, the BET expressions can be further simplified to yield a closed-form analytic solution:

$$C_T = \frac{1}{2}\sigma\int_0^B C_l r^2 \, dr = \frac{1}{2}\sigma C_{L_\alpha}\int_0^B (\theta r^2 - \lambda r) \, dr \tag{10}$$

$$C_T = \frac{1}{2}\sigma C_{L_\alpha}B^2\left(\frac{\theta B}{3} - \frac{1}{2}\sqrt{\frac{CT}{2}}\right) \quad \text{with } \sigma = \frac{N_b c}{\pi R}. \tag{11}$$

Note here, the models presented above describe the thrust of a single rotor. The total vehicle thrust is the sum of the individual rotor thrust

$$T_\Sigma = \sum_{i=1}^4 T_i = \rho A(\Omega R)^2 \sum_{i=1}^4 C_{T_i}. \tag{12}$$

The collective vehicle thrust for the rotor geometry of the quadrotor investigated in this study based on Eqns. 9 and 12 is shown in Fig. 6 (middle) compared to experimental and computational results. A tip loss factor of $B = 0.88$ from Eqn. 8c resulted in the best agreement between the theoretical model and the computational results. This is considerably lower than a B generally used for full-scale helicopter. Note here that the blades also have a substantial root cutout, which could contribute to the low values of B along with the low blade aspect ratio. The solution of the model from Eqn. 9 suggests a near-linear relationship between the pitch angle and the generated thrust of a rotor at high angles of attack and withing the narrow range of pitch angles typically found during hover. Accordingly, simple linear thrust models for a rotor in near-hover have previously been suggested (Refs. [5, 17, 18])

$$T_i = \rho cR^3\Omega^2 C_{L_\alpha}\theta/3. \tag{13}$$

Since the term $\rho cR^3\Omega C_{L_\alpha}$ is constant throughout a test run, this model can be rewritten

$$T_i = b_{L,i}\theta_i, \tag{14}$$

where b_L is a constant combining all rotor parameters, and can also encompass tip losses as well as the effect of the relative inflow angle.

Vortex Ring State Aerodynamics

The vortex ring state (VRS), is a hazardous flight condition, which may arise when a rotor-driven vehicle descends vertically (or at low forward speed) into its own wake. At moderate descent rates of similar magnitude as the induced velocity, the rotor downwash is re-injected through the actuator disk, leading to the formation of a toroidal vortex ring system, which engulfs the entire rotor and can cause a serious loss in aerodynamic lift. It is generally believed that, due to the relative upflow around a rotor and reduced vorticity transport in axial descent, the rotor tip vortices are no longer convected away sufficiently from the rotor disk. Instead, they accumulate to

form the vortex ring system and recirculating flow (Ref. 9). This recirculating and highly unsteady flow can have seriously adverse effects on the rotor aerodynamics, which is why this operating state is generally avoided. Without significantly increasing the rotor power output or pitching the rotor to initiate a sideways motion, the aerodynamic losses associated with the rotor operating in its own recirculating wake can lead to an increase in the aircraft's descent rate, potentially further aggravating the problem. Furthermore, due to periodic rotor wake build up and sporadic break down, rotorcraft experience strong fluctuations in the rotor thrust, manifesting themselves in low-frequency vibrations, which can impair the control authority of the vehicle.

As flow field characteristics in the VRS heavily depend on the induced velocity of the rotor, the primary velocity scale is traditionally chosen as the induced velocity at hover v_h, given by the momentum theory:

$$v_h = \sqrt{\frac{T}{2\rho A}}. \tag{15}$$

Following the momentum theory approach, a rotor's critical axial descent regime, where recirculating flow is expected, can be defined based on the rotor induced velocity and is $-2v_h < v_z < 0$ (Ref. 16). Note here, that the descent velocity, v_z, is defined as negative. This critical descent regime is further divided into the operating states of the vortex ring state and turbulent wake state, based on the nominal flow direction through the rotor. Conventionally, the vortex ring state is defined in the region of $P = T(v_z + v_i) > 0$ (i.e., rotor power is introduced into the flow), whereas power is extracted from the airstream, $P = T(v_z + v_i) < 0$, in the turbulent wake state. The turbulent wake state, with a nominally upwards directed flow direction through the rotor disk $(v_z + v_i) < 0$, is still a highly turbulent flow condition, but levels of recirculation and turbulence are considerably lower than in the vortex ring state. Due to the chaotic flow nature, without a clearly defined rotor flow slipstream, control volume analysis can no longer be applied. Consequently, the basic formulations of the momentum theory do not yield valid results in the region of $-2 < v_z/v_h < 0$. At high descent rates $(v_z < -2v_h)$, the rotor operates in the windmill brake state, where flow is well behaved, with a clearly defined rotor flow slipstream and applicability of the momentum theory.

In the past, the induced velocity of the rotor has been adopted as a general metric to compare rotor performance in axial flight. Because the momentum theory approach loses validity in the vortex ring state (and turbulent wake state), the induced velocity has to be approximated using data from experiments. One approach is using the blade element theory for rigid rotors, which provides an estimate of v_i based on rotor thrust and collective pitch measurements (Ref. 9):

$$\frac{3}{2}(B^2 - r_c^2)\lambda = -\frac{6C_T}{\sigma C_{l_\alpha}} + \theta_{.75}(B^3 - r_c^3)(1 + \frac{3}{2}\mu^2) \tag{16}$$

$$\text{with} \quad \mu = \frac{\sqrt{v_x^2 + v_y^2}}{\Omega R} \tag{17}$$

$$\text{and} \quad \lambda = \frac{v_z + v_i}{\Omega R}. \tag{18}$$

Here, v_x, v_y are the horizontal velocities and v_z is the vertical rotor velocity. For an untwisted rotor: $\theta_{.75} = \theta$. Equations 16-18 can be used to calculate v_i for a given set of rotor parameters and descent rates, which can be compared to empirical VRS models for v_i as a function of v_z, such as (Ref. 9, Table. 3). In practice, the correction factor κ is generally applied to these models to account for additional induced losses with: $v_i = \kappa v_{i,ideal}$. Typically κ is found to be around 1.15 in hover.

EXPERIMENTAL APPARATUS

Free-flight experiments were performed on a variable-pitch quadrotor within a vertical wind tunnel to investigate the VRS aerodynamics and characterize the relative thrust loss for this type of rotorcraft. The following section provides a comprehensive description of the rotorcraft platform and equipment utilized throughout the study.

Rotorcraft

A modified *Stingray 500* quadrotor (see Fig. 2) was used as the test platform in this study. This commercial-off-the-shelf product, generally used for aerial acrobatics, is equipped with independent pitch control for each rotor within the range of approximately $-35° < \theta < 35°$. Unlike conventional fixed-pitch multirotors, which are controlled via differential rotor speed, this vehicle is powered by a single electric motor, driving all four rotors via a belt and pulley transmission system at the same, constant rotation rate of 6316 RPM. The vehicle has a total mass of 1.68 kg, including all onboard equipment added for this experiment and the major dimensions are illustrated in Fig. 2. While the drivetrain of the *Stingray 500* (motor, belt-pulley-system, rotor blades, rotor shafts, and swashplates) was left unchanged, the central fuselage was modified to incorporate a *Pixhawk* flight controller (FC), a *Raspberry Pi* onboard computer, and an electric RPM sensor. The battery position was adjusted to align the center of gravity with the vehicle's geometric center. Furthermore, motion capture markers were placed on the craft to allow for rigid body tracking of the vehicle within the laboratory space. All relevant vehicle and rotor parameters are also listed in Table 1 and compared to the Ingenuity Mars Helicopter and the Mars Highland Helicopter (MHH) designed by NASA Ames (Ref. 3).

Rotor Blade Pitch Control

The pitch of each rotor on the Stingray can be independently controlled by separate swashplates, allowing positive as well
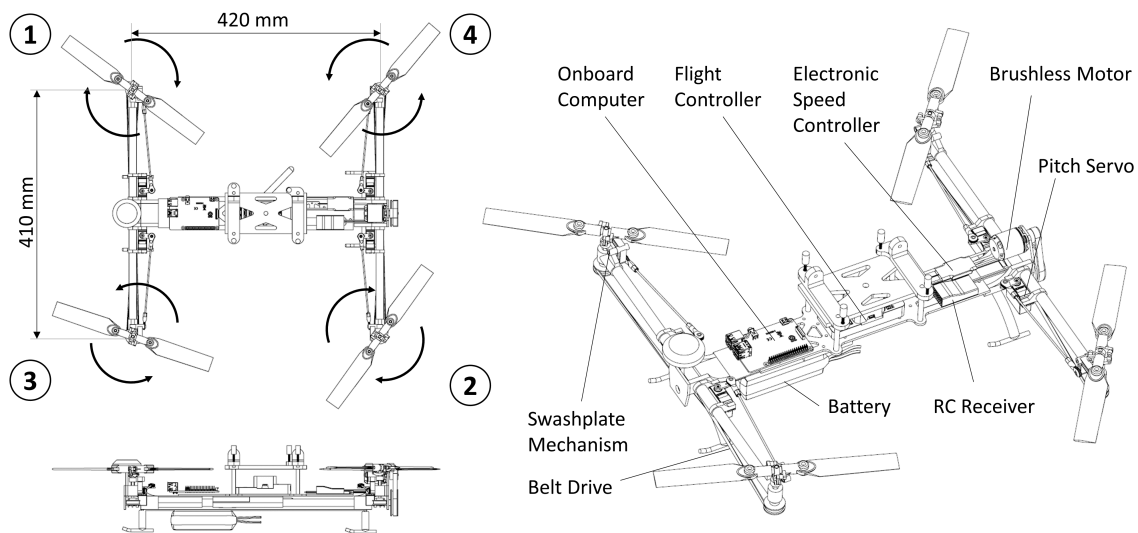
Figure 2. Variable-pitch quadrotor platform including major dimensions, rotor number assignment, and component description.

as negative blade pitch angles. During this study, the rotor pitch was limited to positive angles only for a better representation of future Mars helicopter concepts which were deemed unlikely to require acrobatic powered-descent. Each swashplate is actuated by a servos via pushrods, which is mounted on the rotor arms, close to the fuselage (see Fig. 2). Because only collective and no cyclic rotor pitch control is employed, a single servo per rotor is sufficient to raise or lower the swashplate for increasing or decreasing blade pitch, respectively. Each servo position is controlled by the flight controller via a pulse width modulated (PWM) signal with increasing pulse width length resulting in a counter-clockwise servo rotation. Servo arms and pushrods were adjusted such that a 1.5 millisecond pulse corresponded to a 90-degree servo position and approximately zero rotor pitch. Figure 3 shows the individual rotor pitch vs. PWM signal, which was measured using a RC pitch gauge temporarily installed on the rotor. Given the installation orientation of each servo, either a counter-clockwise (servos 1 and 2) or clockwise (servos 3 and 4) rotation direction is needed to increase the blade pitch. The figure indicates that for a wide range of pitch angles, which are also typically found during regular operation, a near-linear relationship exists between the PWM signal and pitch. It's important to note here, that the swashplate mechanism itself has a significant backlash of $\pm 2°$ for a given PWM input as indicated by the pitch gauge. Furthermore, installing the pitch gauge generally caused a natural pitching up of the rotor blade within this backlash range due to shifting the center of gravity behind the blade's mounting location. Thus, the measurements in Fig. 3 were expected to be marginally overestimating the rotor pitch for a given PWM signal, as reflected by the error bars extending further towards lower pitch values. It could later be confirmed that the experimentally determined pitch angles were approximately 1° higher than the theoretical and computational ones. Given the uncertainty in the rotor pitch measurements, the raw PWM values were used directly to es-

timate the in-flight rotor thrust.

Rotor Geometry

Figure 4 displays the geometry of the rotor blades. These dimensions were obtained by manual measurements since no official manufacturer specifications for the rotor geometry was available. Each rotor is equipped with two rotor blades and has a diameter of 286 mm (∼11.3 inches). The rotor blades are untwisted, marginally linearly tapered between stations A and B, and have symmetric airfoils. Maximum thickness and chord length were measured for stations A and B. All relevant rotor parameters are also listed in Table 1. Inboard of station A, the rotor blade has a more complex shape with the flat mounting face (indicated as the hatched area) protruding from the blade surface. It is worth mentioning that defining the rotor solidity, σ, for these low aspect ratio rotor blades can be quite sensitive to the selection of the appropriate blade
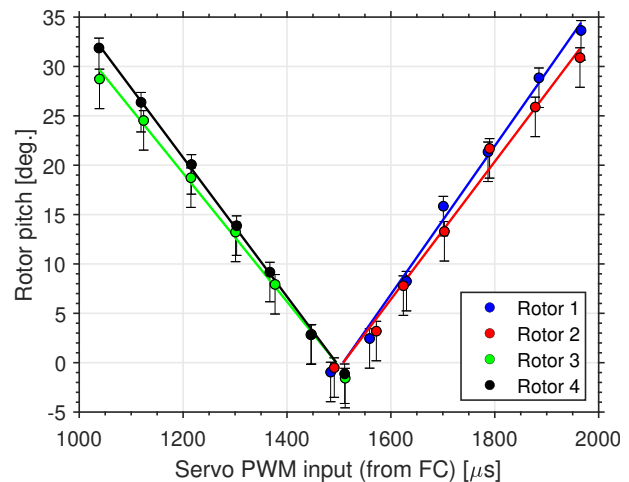
Figure 3. Rotor pitch measurements based on pulse width modulated servo signals.
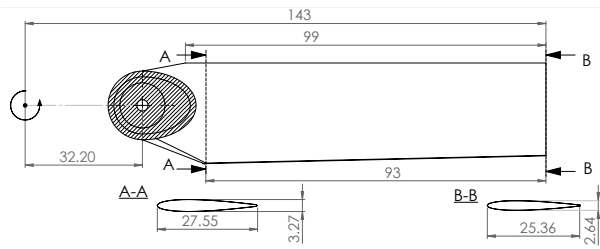
Figure 4. Rotor blade geometry based on manual measurements in mm (hatched area: un-profiled, flat hub mounting face).

planform area. In this case the rotor solidity was based on the blade's profiled area, thus, excluding the mounting face (hatched area). For simplicity, the computational approach approximated the rotor blade geometry inboard of station A as a constant chord rotor up to the rotor mounting hole at $r = 32.2$ mm, and also assumed a NACA0012 airfoil throughout the blade.

Wind Tunnel Setup and Experimental Procedure

Figure 5 schematically depicts the setup of the experimental campaign. A multi-fan wind tunnel facility at the Center for Autonomous Systems and Technologies (CAST) at Caltech was used to simulate the external upflow of axial descent. This allowed to study the rotorcraft's VRS performance in a controlled laboratory setting. The wind tunnel facility is composed of 1296 individual DC fan units, which were all assigned identical duty cycles for a uniform flow, and is capable of generating flow velocities between 0 - 14 m/s. The test section has an overall cross-sectional area of 2.88 m × 2.88 m (9.5 ft × 9.5 ft) and can be oriented horizontally as well as vertically. An external motion capture system installed around the wind tunnel, furthermore, provided precise three-dimensional position and attitude information of the quadrotor during flight by tracking the dedicated infrared markers.

A total of five free-flight tests were performed over the wind tunnel. During each test, the rotorcraft was manually piloted and hovered approximately 4 m (13.1 ft) above the vertical wind tunnel. The rotor pitch was adjusted based on a combination of manual control inputs and FC commands to maintain a constant position as well as level attitudes over the wind tunnel. After an initial hover period, the wind tunnel freestream velocity, v_{WT}, simulating the external flow of a steady descent, was incrementally increased in 20 second intervals up to a maximum wind tunnel velocity of approximately 6 m/s. During the test flight, the onboard computer, running a version of ROS (Robotic Operating System) logged all relevant vehicle operational parameters at a sampling frequency of approximately 30 Hz, including rotor rotation rates, pitch servo signals (PWM), acceleration measurements by the onboard inertial measurement unit (IMU), and position as well as attitude information provided by the motion capture system. All parameters were time-stamped and streamed back to a central control station via a WIFI link.
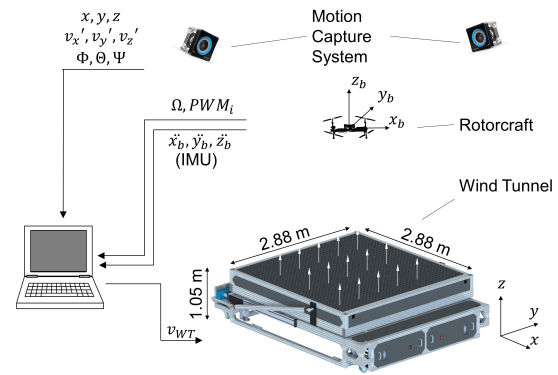
Figure 5. Schematic wind tunnel setup and data pipelines (wind tunnel schematic provided by *WindShape LLC*).

APPLICABILITY OF RESEARCH

Direct Applicability

All experimental and computational efforts of this study have been performed under standard atmospheric conditions ($\rho = 1.225$ kg/m^3, $g = 9.81$ m/s^2). Consequently, findings are directly applicable to conventional rotorcraft operation under Earth-relevant scenarios. Specifically, the research presented here addresses terrestrial low Reynolds number, variable-pitch multirotor aerodynamics in axial descent.

Similarity Considerations for Future Mars Mission

Because the study was motivated by the investigation of MAD in the Martian atmosphere, the applicability of results for potential future Mars missions is here closer examined. For this, a comparison of the Stingray's key geometric and operational parameters to the current Ingenuity system of the Mars 2020 mission and the proposed Mars Highland Helicopter (MHH) is shown in Table 1. In the past, vacuum chamber experiments with a similar wind tunnel facility were used for Ingenuity, to avoid the challenge of aerodynamically scaling the problem. However, this chamber was not available for this research project. Yet, even though experiments and computations were performed under Earth-relevant conditions, appropriate scaling of physical parameters can help translate results and make them applicable to Martian scenarios. For this, fundamental requirements are generally the geometric (i.e., identical design) and dynamic similarity (Reynolds number and Mach number, among others) between engineering models and the final design. However, in practice, it is generally challenging to represent all relevant variables appropriately, which is why it is advisable to establish an order of priority of the scaling requirements based on the objectives of the experimental campaign.

Because the experiments were primarily used to address variable-pitch multirotor aerodynamics in the VRS, special emphasis was given towards similarity requirements of rotor parameters in axial descent. As previously stated, axial descent is primarily parameterized by the ratio of the descent speed, v_z, to rotor induced velocity and v_h was given

as the appropriate velocity scale (Ref. 9). Thus, the ratio v_z/v_h was considered the primary focus for non-dimensional matching between the Mars case and the Earth-analog experiment. For reference, the MHH, deployed at the end of the parachuted phase at 30 m/s, would experience a descent rate ratio of $v_z/v_h \approx -1.16$. Accordingly, for descent-rate-ratio equivalence, simulated descent velocities of up to ~ 6 m/s ($v_z/v_h \approx -1.17$) were investigated during the Earth-relevant study of the Stingray.

Further considerations should be given to the rotor and vehicle geometry as well as Reynolds number and Mach number, all of which have been reported to have a secondary significance on the axial descent performance of a rotorcraft. Currently, no official design for a future Mars science rotorcraft exists, but the finalized design is likely to be a variable-pitch multirotor platform. Thus, a variable-pitch quadrotor was chosen as most suitable to help inform about control-related issues and was assumed to be sufficiently close to any future Mars science helicopter design for validating Mars flight simulation tools.

Satisfying full dynamic similarity can be challenging in this case, since the Mars rotorcraft platforms generally operate at a relatively low Reynolds number ($\sim 10^4$), and a high Mach number ($\sim 0.7 - 0.8$) compared Earth-relevant systems, due to the low atmospheric density. While increasing rotation rates increases the Ma number, it will also simultaneously increase the Re number. Hence, it is generally not possible to match both Re and Ma using Earth-equivalent conditions without simulating the appropriate atmosphere. Ultimately, the Re number was presumed to have a greater significance on the flow characteristics and rotation rates were chosen as low as possible to minimize the Re number differences between the Stingray experiments and Mars rotorcraft.

Altogether, in the context of the test campaign, the descent rate ratio, v_z/v_h, was seen as the most critical non-dimensional variable, which is the primary influencing factor of rotorcraft descent aerodynamics. Therefore, matching the descent rate ratio was believed to give a suitable representation of axial descent conditions on Mars in this first-order approach. Mean-

Table 1. Key vehicle parameters of the Stingray compared to the current Ingenuity system and proposed Mars Highland Helicopter (MHH).

Parameter	Stingray	Ingenuity[a]	MHH[b]
Vehicle Mass, m	1.68 kg	1.80 kg	4.14 kg
Rotor Radius, R	0.143 m	0.605 m	0.605 m
No. of Rotors, N_r	4	2	2
No. of Blades/Rotor, N_b	2	2	4
Rotor Solidity, σ	0.0893	0.148	0.404
Rotation Rate, Ω	6316 RPM	2575 RPM	2882 RPM
Tip Speed, v_{tip}	94.6 m/s	163 m/s	183 m/s
Ma_{tip}	0.28	0.71	0.8
Re_{tip}	1.61×10^5	2.19×10^4	3.37×10^4
Hover Velocity, v_h	5.12 m/s	17.0 m/s	25.8 m/s
Descent Velocity, v_z	≥ -6 m/s	-	-30 m/s
Descent Rate Ratio, v_z/v_h	≥ -1.17	-	-1.16

[a] (Refs. 1, 4)

[b] (Ref. 3)

while, the impact of geometry and other non-dimensional parameters (Re, Ma) is secondary, and future, more sophisticated studies should seek to minimize the geometric and dynamic differences to the actual Mars scenario. However, this may require dedicated environmental chambers to scale Reynolds number and Mach number appropriately and simultaneously.

EXPERIMENTAL HOVER THRUST CALIBRATION

Since the experimental campaign was based on free-flight tests, the generated rotor forces could not be measured directly, but had to be inferred from in-flight vehicle parameters. In this case, two separate approaches were used to determine the vehicle thrust, one based on vehicle acceleration data by the IMU and one based on PWM values sent to the pitch-actuation-servos. Both methods provided an independent assessment of the total vehicle thrust and could be compared against each other to characterize the relative vehicle performance in axial descent.

Using the vehicle mass and accelerations along the vertical axis, the forces acting on the craft and causing said acceleration could easily be calculated. In theory, assuming negligible fuselage drag and other external forces acting on the rotorcraft, this thrust measurement corresponds to the instantaneous combined vehicle thrust, independent of the flight conditions. Since the acceleration data is directly measured by the onboard IMU, the thrust value based on this method is referred to as the measured thrust, T_m.

In addition, the thrust of a rotor can be approximated based on the rotor blade pitch angle, θ, using the linear model suggested in Eqn. 14 ($T = f(\theta)$). Since this model is only valid for near-hover conditions, the thrust values predicted by this method correspond to the thrust, which the vehicle would be generating for a set of pitch angles if under hover conditions. Because this value is not measured directly, but estimated from operational parameters, this thrust value is here referred to as estimated thrust, T_θ. In summary:

$$\begin{aligned} T_m &\approx T \\ T_\theta &\approx T_h \end{aligned} \tag{19}$$

and under near-hover conditions, the estimated total rotor thrust, T_θ, equals the measured thrust, T_m. Following the linear model for the individual rotor thrust based on the geometric pitch angle from Eqn. 14
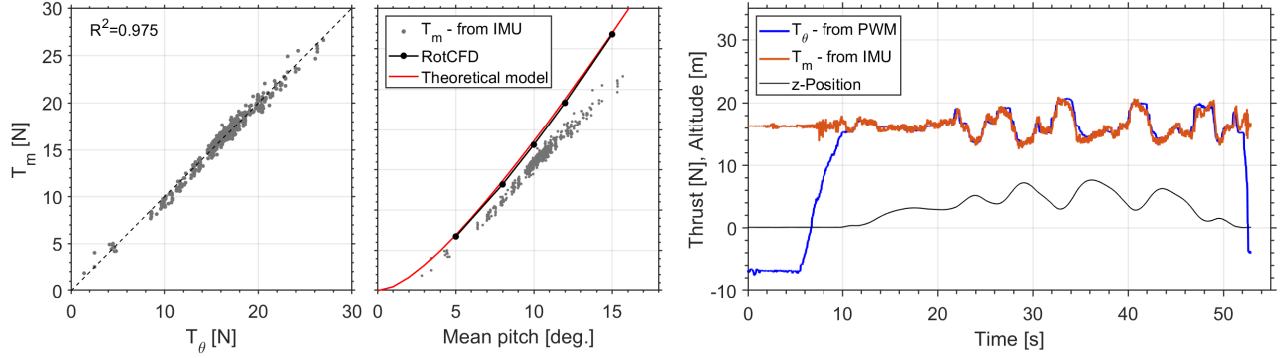
$$T_m = T_\theta \qquad \text{at hover} \tag{20}$$

$$T_\theta = \sum_{i=1}^{4} b_{L,i}\theta_i \tag{21}$$

$$T_m = m\ddot{z}_b \tag{22}$$

where $\ddot{z}_b$ is the acceleration in the body frame and $b_{L,i}$ are constants for each rotor. While the operational parameters are known and theoretical values for $C_{L\alpha,i}$ technically exists

Figure 6. Results of the hover thrust calibration (flights without wind tunnel use); estimated vs measured thrust based on training data (left), mean pitch angle of all four rotors vs measured thrust (middle), and time series of a test set flight (right).

to approximate $b_{L,i}$, it is most convenient to directly determine these constants from experimental data by means of least squares fitting. This can also significantly improve the accuracy of the thrust estimation. Here, instead of using the less accurate rotor pitch measurements, the PWM signal (see Fig. 3) was utilized to find the estimated thrust with:

$$\theta_i = a_i PWM_i + b_i \qquad (23)$$

where a_i and b_i are constant for each rotor. As a result, Eqn. 21 becomes:

$$T_\theta = \sum_{i=1}^{4} a_i PWM_i + b_i \qquad (24)$$

Note here that the factor $b_{L,i}$ has been absorbed into the constants. Furthermore, the constant term b_i was removed here by applying the simplifying assumption (see Fig. 3)

$$b_4 = -b_1 \qquad \& \qquad b_3 = -b_2 \qquad (25)$$

which has proven to result in no significant loss of accuracy, reducing the linear model to estimate the rotor thrust based on the pulse with modulated signal sent to the servos to:

$$T_\theta = \sum_{i=1}^{4} a_i PWM_i \qquad (26)$$

To generate the training data for the least squares fitting, three free flights with purely axial trajectories and without wind tunnel usage were performed. The craft stayed horizontal throughout the flight and PWM as well as IMU data was recorded at a sampling rate of 30 Hz. The goal of these flights was to generate parameter sets with a wide range in PWM values and thrust levels, which can be achieved by vertical acceleration/deceleration of the craft. For better results, only data points close to hover conditions ($0\,\mathrm{m/s} < v_z < 2\,\mathrm{m/s}$) were considered during fitting to not introduce VRS and rapid ascent aerodynamics. Altogether, a total of approximately $n = 1000$ data points distributed over the three flights were collected and used for fitting the coefficients.

Figure 6 illustrates the results of the experimental calibration campaign. The developed linear regression model on the

left indicates a good agreement ($R^2 = 0.975$) between the observations (T_m, based on IMU data) and the expected values (T_θ, based on the regression for the given PWM values) under near-hover conditions. As previously stated, the constant term removed in Eqn. 25 or expanding the model by adding quadratic terms to the linear regression model in Eqn. 26 did not improve the quality of the fit. Figure 6 (middle) shows the mean rotor pitch vs. measured total thrust of the vehicle, T_m, for all data points obtained during the three flights. The experimental results are close to the computational RotCFD data and theoretical results; however, the experimental pitch angles were consistently 1° higher for a given thrust. This offset was largely attributed to the backlash in the swashplate design and was corrected for in the following, where necessary. Note here that the thrust measurements are not impacted by the backlash, since the linear regression model for T_θ uses the PWM values as the independent variable without any consideration of the actual rotor pitch measurements.

The time series of a separate validation flight with a similar axial flight trajectory (Fig. 6 (right)) shows that the estimated thrust is in good agreement with the measured thrust during the time of flight ($10\,\mathrm{s} - 50\,\mathrm{s}$). Both values match particularly well during hover ($15\,\mathrm{s} - 20\,\mathrm{s}$) and the dynamic events at the later stage of the flight are also captured to a reasonable accuracy.

Both the estimated and measured thrust were subsequently used for the investigation of the quadrotor's performance in descent, where the rotor performance is predicted to deviate from hover due to prevailing VRS aerodynamics. Therefore, the thrust values were expected to likewise deviate from one another in axial descent, with the measured thrust corresponding to the true vehicle thrust while the estimated thrust served as a reference case for hover conditions.

EXPERIMENTAL AXIAL DESCENT RESULTS

A total of five flights under simulated descent conditions were conducted with a key focus on the thrust loss occurring during

the vortex ring state compared to hover conditions. Figure 7 illustrates the raw vehicle data ($f_s = 30\,\mathrm{Hz}$) of one selected flight with the rotorcraft hovering over the vertical wind tunnel at an altitude of approximately 5 m. Wind tunnel velocities were incrementally increased with time, from 0 to a maximum of 6 m/s; higher descent rates were not feasible due to reduced controllability of the aircraft. Even though the position was intended to be stationary within the wind tunnel flow, minor movements of the piloted vehicle were inevitable, as seen in the altitude data. For correctness, any additional rotorcraft vertical motion was accounted for and was added to the wind tunnel velocity for a net simulated descent velocity, $v_z = v_z' - v_{WT}$. Here $\mathbf{v}'$ denotes the vehicle velocity vector in the laboratory frame relative to the wind tunnel, and v_{WT} the wind tunnel freestream velocity. This notation was selected to avoid confusion between the vehicle velocity v_z' and the net simulated descent velocity v_z. It should be noted that v_z is negative in descent, but is graphed as absolute values, $|v_z|$, in Fig. 7 for ease of plotting.

Figure 7 indicates that during hover and at low descent rates, the measured and estimated thrust agree well and are nearly identical, which is expected, given that the calibration for T_θ was performed under near-hover conditions. However, as descent rates increase, the values increasingly deviate from one another, with T_θ exceeding T_m. The time series of both thrust signals, furthermore, show that the fluctuations become increasingly pronounced at higher descent rates. A similar increasing trend with descent rate is found when inspecting the roll and pitch angle of the vehicle. While these attitude fluctuations are limited to $\pm 2°$ during hover, oscillations in excess of $\pm 10°$ occur at descent rates of 6 m/s.
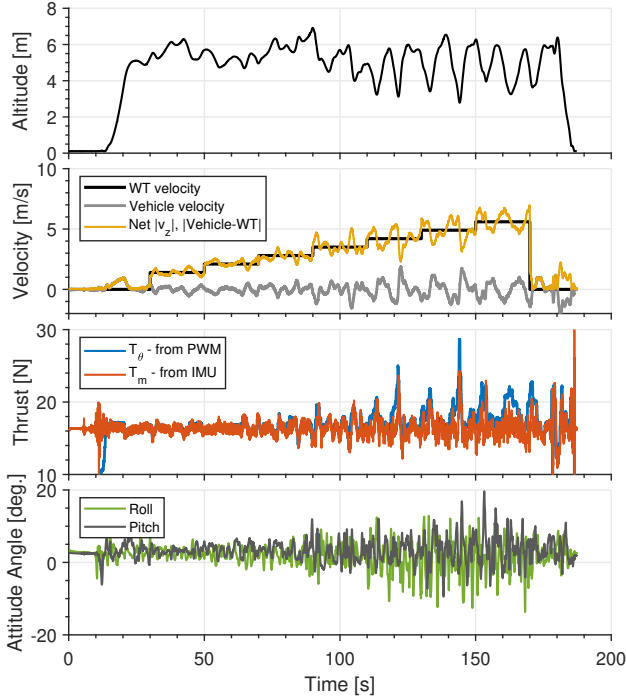
Figure 7. Raw in-flight data of a selected test flight with increasing wind tunnel velocity (Flight 2).
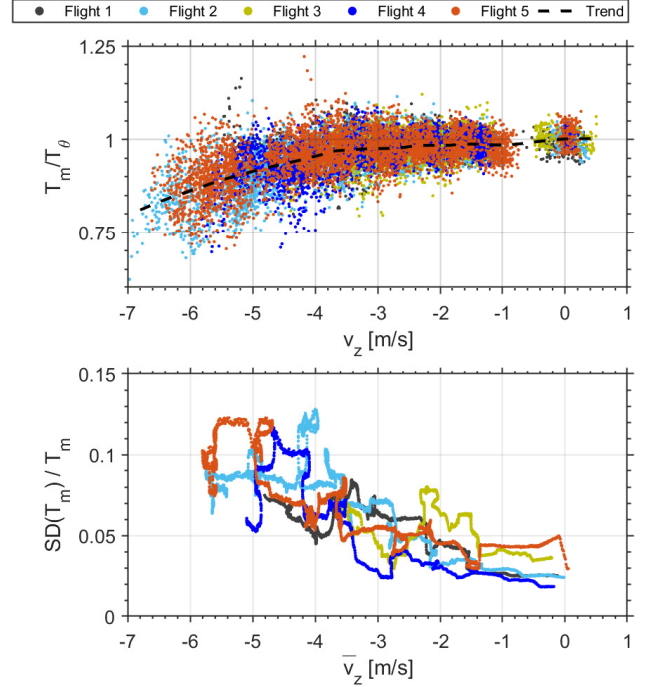
Figure 8. Relative thrust loss and normalized thrust standard deviation as a function of descent rate.

For quantitative evaluation of the vehicle performance in descent, all raw data sets were post-processed to exclude wind tunnel ramp-ups, the take-off, and landing process and were analyzed as a function of descent velocity. In total, approximately 14,700 data points were collected across all five flights. Figure 8 shows the ratio of measured over estimated thrust T_m/T_θ and the normalized standard deviation of the measured thrust, $SD(T_m)/T_m$, as a function of the descent velocity. This processed data shows a significant amount of scatter, which can be attributed to the inherent noise in IMU measurements and the unsteadiness arising from undergoing VRS conditions. Despite the scatter in these observations, clear trends can be identified: as the descent velocity increases, the ratio of the measured thrust over the estimated thrust decreases monotonically to a minimum of $T_m/T_\theta = 0.8$ at $v_z = -6.5\,\mathrm{m/s}$ ($v_z/v_h \approx -1.2$), suggesting that thrust losses of up to 20% compared to hover conditions occur at this descent rate. Physically speaking, these results indicate that maintaining a constant thrust equal to the vehicle weight ($T = T_m = mg$) for hovering in the vertical airflow requires a greater rotor pitch compared to that for hover conditions. Therefore, $T_\theta \approx T_h$ increases with descent rate due to the increase in rotor pitch, while the true thrust T_m remains near-constant. Vice versa, if maintaining a constant RPM and rotor pitch (i.e. constant T_θ) the rotorcraft is expected to generate less thrust, T_m, with increasing descent rate due to the aerodynamic disturbances associated with the VRS. This thrust loss of up to 20% is considerable and will increase the descent rate further; thereby aggravating the problem. It is worth mentioning that the vehicle drag has been assumed negligible throughout the investigation. In reality, the drag of the vehicle fuselage due to the

wind tunnel flow adds to the thrust value T_m, while T_θ is left unaffected. Thus, if corrected for the vehicle drag, the values for T_m are expected to be reduced slightly, resulting in even lower values of T_m/T_θ.

These results regarding rotor performance in the VRS are largely consistent with previous experimental research, which have reported maximum thrust losses in vertical descent of comparable magnitude occurring descent rate ratios of $v_z/v_h = -1.2$, both for variable-pitch rotors (Ref. 12) as well as for fixed pitch rotors (Ref. 11). For the case of variable-pitch rotors, an increased pitch was similarly required to maintain a constant thrust in vertical descent. Thus, following these studies, the ratio of T_m/T_θ is expected to recover at higher descent rates when entering the turbulent wake and windmill brake state (Ref. 9). However, higher descent rates could not be investigated during this experimental campaign due to decreasing controllability with increasing descent rate, which did not allow for the craft's safe operation beyond this 6 m/s. The investigation of higher descent rates is targeted in future studies. Moreover, the question of how the rotor pitch influences the maximum losses could not be investigated here independently given the constraints imposed by the free-flight campaign, but is discussed in more detail in the computational result section.

In addition to an average loss of rotor thrust, the vehicle experiences strong thrust fluctuations and attitude oscillations, indicated by the normalized standard deviation of the thrust, $SD(T_m)/T_m$, in Fig. 8 and qualitatively by the vehicle pitch and roll information in Fig. 7. In this case, $SD(T_m)$ was determined as the moving standard deviation of the T_m-time-series for each flight and was calculated over a sliding window with a length of 300-data-point, corresponding to a 10 s interval. The computed values are normalized by the mean thrust over the sliding window and are plotted over the mean velocity over said window, $\overline{v_z}$. The normalized standard deviation can be observed to increase fourfold, from $SD(T_m)/T_m = 0.025$ at $v_z = 0$ to $SD(T_m)/T_m = 0.1$, which is considerable. Given a flight-data sampling rate of 30 Hz, this data does not allow the capture of higher frequency content above 15 Hz, far lower than the rotor rotation rate of 105 Hz. However, VRS behavior has been reported to manifest itself in characteristically low frequency thrust fluctuations on the order of multiple rotor rotations (Refs. 11, 16), which appear to be captured here. Similarly, growing vehicle roll and pitch oscillations are introduced with increasing descent rate, even though the flight controller is enforcing a level attitude. This can directly be explained by asynchronous thrust fluctuations occurring at the various rotors. While these measured attitude information are assumed to be highly vehicle specific, they can serve as a qualitative metric of vehicle stability as a function of descent rate, suggesting that the stability and controllability of a rotorcraft can seriously be impaired by prevailing VRS aerodynamics.

For comparison of the experimental results to established models of the VRS, the rotor induced velocity, v_i, was calculated via Eqn. 16 ($B = 0.88$) based on the measured vehicle thrust $T = T_m = m\ddot{z}_b$ and the rotor pitch. In this case, the rotor
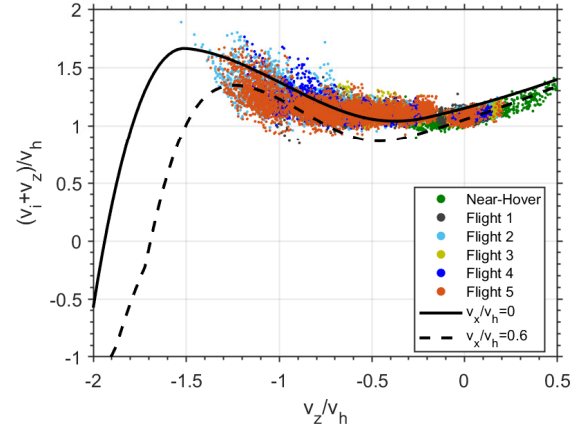

Figure 9. Comparison of experimental data with the VRS model by Johnson (Ref. 9) for axial and non-axial flight conditions.

pitch was averaged across all rotors and corrected for the apparent offset introduced by the imprecise pitch angle measurements as indicated in Fig. 6 ($\theta = \bar{\theta} - 1$ deg). All lateral vehicle movements were accounted for via $\mu = \sqrt{v_x'^2 + v_y'^2}/(\Omega R)$ and v_z' was previously accounted for and added to the wind tunnel velocity ($v_z = v_z' - v_{WT}$). Figure 9 plots the calculated values of $(v_i + v_z)/v_h$ over the descent rate ratio v_z/v_h for all experimentally collected data points and compares them to an established model of the VRS as suggested by Johnson (Ref. 9, Table 3) using a $\kappa = 1.15$. Results are generally in agreement regarding magnitudes of the induced velocity and development with increasing descent rate. While small discrepancies can be found, such as a less pronounced local minimum in the presented experimental data at $v_z/v_h = 0.5$, it appears that previously established models regarding the VRS performance of helicopters generally apply to these low Reynolds number multirotor configurations as well.

CFD SIMULATION

The mid-fidelity computational fluid dynamics (CFD) program RotCFD (Rotorcraft CFD), developed by Sukra Helitek, Inc., was used to generate computational predictions of the rotor performance and body forces and moments analogous to the experiments. RotCFD has several modules that allow rotorcraft performance metrics and flow fields to be simulated over time and analyzed in a Graphical User Interface (GUI). This analysis uses the Rotorcraft Unstructured Solver (RotUNS) module which uses three-dimensional, Unsteady Reynolds Averaged Navier-Stokes equations (URANS) on a Cartesian unstructured grid with tetrahedral body-fitting near the body (Ref. 19). The rotor blades are modeled using the blade element method (BEM) and are represented through the momentum they impart on the flow. The URANS equations provide the flow field near the rotors using the rotor induced momentum sources and the blade element theory provides the forces on the rotor blades from the local velocity vector field. These equations are coupled implicitly to yield a
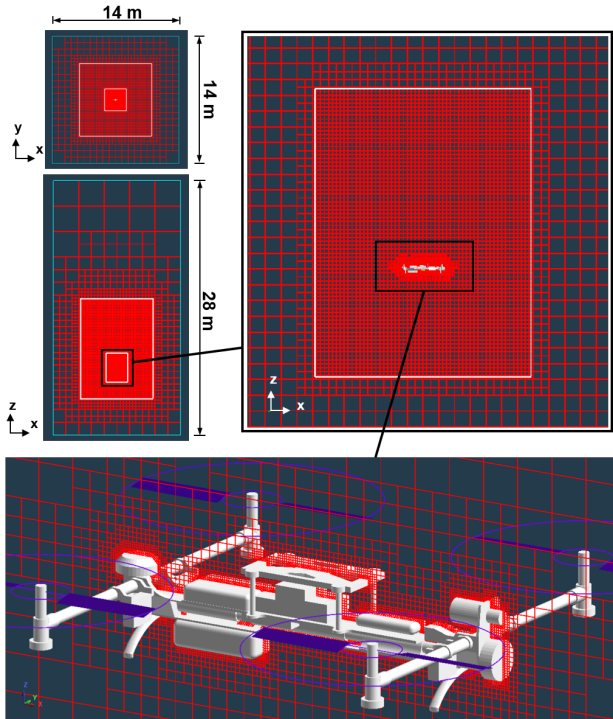
Figure 10. Computational domain and model used in the RotCFD simulations.

self-contained method for generating unsteady performance, as well as the near and far wake including all the aerodynamic interferences present (Ref. 14). Additionally, RotCFD has SIMPLER, Semi-Implicit Method for Pressure-Linked Equations Revised, which is a line of pressure based algorithms used with the under relaxation factors to iteratively compute the flow field. Turbulence is accounted for by the URANS equations combined with a two-equation realizable $k - \varepsilon$ turbulence model with special wall treatment (Ref. 19).

In a precursor to this work (Ref. 3), RotCDF was used to study the mid-air release of a co-axial rotorcraft from an entry backshell under Mars-like conditions. Previously, RotCFD had also been validated against experimental test data of similar problems to the one being studied in this paper, such as forward flight of multirotor configurations (Ref. 20) as well as isolated rotor performance at Martian atmospheric densities (Refs. 21, 22).

For accurate representation of the experiments, a CAD model of the Stingray was created and imported into RotCFD. The CAD model was kept as close to the original Stingray as possible, yet small simplifications were made to reduce computational complexity. The internal grid generator, UGen, was used to generate a Cartesian octree grid, starting from the boundary and then intersecting the body. The cells that intersect the geometry and the surrounding cells are sub-divided into tetrahedra, resulting in a grid that approximately conforms to the surface of the body. The objective, when defining the grid parameters, was to find a balance between the accuracy of the results, computational budget, and time availability. However, increasing the refinement of the grid did not always seem to yield more accurate results. Several grid stud-

ies were performed to ensure that the grid around the body of the Stingray and the rotors were refined enough to provide realistic results, while not overtaxing the computer (limited by ~ 2 million cells), and also not biasing the flow field. The final grid with the simplified Stingray body, is illustrated in Fig. 10. It can also be seen in Fig. 16 that the refinement boxes did not bias the flow field, i.e. there is no drastic change in the flow field at the boundaries of the refinement boxes. Care was taken to ensure that the grid remained the same throughout all cases in order to reduce the potential of additional inaccuracies and to increase the confidence in the comparisons between cases.

The physical simulation time and the number of timesteps varied for each case, however the ratio of timesteps to simulation time remained the same, i.e. 100 timesteps per second. The simulation time was increased until a reasonable convergence for the forces and moments on the Stingray was reached. In all computational runs, the rotor operational parameters matched the experimental testing conditions with the same rotor radius $R = 0.143$ m, running at a tipspeed of 94.6 m/s, and the descent rate and collective were varied from 0 m/s to 6 m/s and 5 deg to 15 deg, respectively. As previously indicated in the Experimental Apparatus section, the rotor blade geometry was approximated in RotCFD as an untwisted blade with a NACA0012 airfoil. The chord inboard of station A (compare with Fig. 4) was kept constant up to the root cutout ($r_c = 0.225$) and the blade was linearly tapered between station A and B. Table 2 provides an overview of the chord length at the relevant stations. To further reduce computational com-

Table 2. Chord length at characteristic blade stations based on the approximated rotor geometry used in RotCFD.

r/R	0.225 (r_c)	0.350 (A)	1 (B)
c/R	0.193	0.193	0.177

plexity, the vehicle attitude was constrained to remain level at all times, with the rotor planes perpendicular to the simulated freestream flow of axial descent, while moments on the vehicle could still be observed. It is important to mention that RotCFD did not include a feedback loop for thrust matching, i.e. to maintain a constant thrust independent of the simulated descent rate by actively varying the rotor pitch, similar to the experiments. Instead, the rotor pitch was fixed at selected angles and changes to the overall vehicle thrust for different descent rates were examined.

Rotor Performance Analysis

A total of 20 simulations were performed in RotCFD, at rotor pitch angles of $\theta = 5°, 8°, 10°, 12°, 15°$ under hover conditions ($v_z = 0$), and $\theta = 8°, 10°, 12°$ at descent velocities within the range of -6 m/s $< v_z < -1$ m/s. Figure 11 depicts the results of all computationally investigated configurations. Plotted here is the combined total vehicle thrust of all four rotors

as a function of descent speed. These thrust results represent the quasi-steady-state solution, similar to the mean rotor thrust in descent without the strong rotor thrust fluctuations. These results are qualitatively in agreement with the experimental study, where the rotor thrust falls below the performance at hover as descent rate increases, regardless of the rotor pitch. Because operational parameters (rotor pitch and RPM) remain constant along the curves, these thrust losses are presumed to stem from the aerodynamic losses caused by the rotors operating in their own recirculating wake. At higher descent velocities the thrust undergoes a recovery for all pitch angles, which is assumed to be due to the rotorcraft leaving VRS and entering the turbulent wake state. In terms of absolute quantities, the critical descent rate, where the thrust minimum occurs, increases with rotor pitch or alternatively, with rotor thrust. To account for the varying rotor thrust with rotor pitch, Fig. 11 (bottom) represents the normalized thrust curves for the investigated rotor pitch angles. Interestingly, the local minimum of all curves is consistently found at the same normalized descent rate ratio of $v_z/v_h = -0.65$, despite varying rotor pitch and vehicle thrust, supporting the hypothesis that the induced velocity can indeed be considered the primary scaling of VRS aerodynamics. Yet, while the location of the minimum remains unchained, the extent of the thrust loss appears to reduce when the rotor pitch is increased. This indicates a secondary influence introduced by the collective pitch of a rotor, with higher pitch angles resulting in improved performance during VRS, which is consistent with previously reported experimental test data (Refs. 10, 13). Note here that this observation is based on a limited number of discrete data points and additional computational efforts with higher sampling density are needed to confirm these findings. However, given the considerable curve divergence at the local minimum, these findings are expected to not change qualitatively.

Comparison to Experiments

A primary interest of performing a duplicate computational study alongside the experiments was to evaluate the fidelity and limitations of simulating axial descent using RotCFD, as the computations can ultimately be adapted for Martian applications with relative ease. To do so, the thrust losses found in both studies were compared.

However, it has to be kept in mind that both studies followed different investigative strategies. During experiments, a constant vehicle thrust was maintained by varying the rotor pitch for continuous hover over the wind tunnel. In RotCFD, the rotor pitch was fixed instead, resulting in a changing vehicle thrust. Hence, prior to directly comparing the results, a conversion of either data is required. Simply normalizing the data similar to Fig. 11 (bottom) will account for differences in the rotor thrust or the induced velocity, however, the previously discussed secondary effects of the rotor pitch would be lost. Hence, the RotCFD data was converted from $\theta = const.$ to $T = const.$. This was done by determining the relative thrust loss as a function of vehicle thrust and descent rate $(T/T_h = f(v_z, T))$ using the discrete RotCFD data points. Fig-
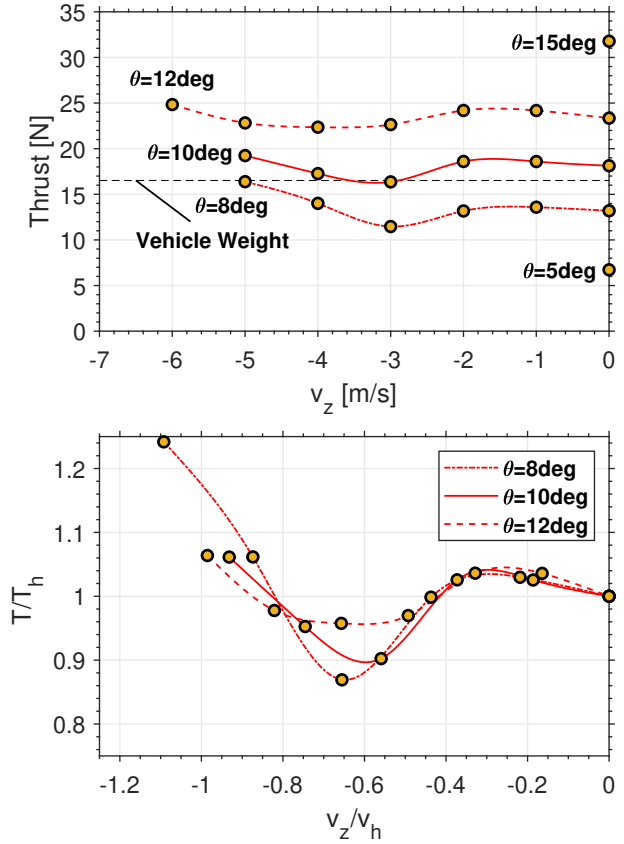
Figure 11. Total vehicle thrust as a function of descent rate and rotor pitch of all investigated cases using RotCFD.

ure 12 (top) depicts the interpolated results of the relative rotor thrust. This approach allows to account for the shifting of the local thrust minimum towards higher descent velocities at higher thrust, as well as the reduced thrust minimum at higher pitch angles. Using these results, the relative thrust loss based on RotCFD data can be estimated for $T = mg = const.$, by extracting the interpolated values along the dashed line. These results can then be directly compared to the experimental data.

A comparison is shown in Fig. 12 (bottom). Even though the experiments and computations both indicate a loss in thrust with increasing descent rate, the trends of the relative thrust are quite dissimilar. The local thrust minimum with subsequent recovery in the RotCFD data is found at $v_z = -3\,\mathrm{m/s}$, with overall thrust losses $(T/T_h < 1)$ between $-4\,\mathrm{m/s} < v_z < -2\,\mathrm{m/s}$, whereas the experimental values monotonically decrease up to $v_z = -6\,\mathrm{m/s}$ without any indication of recovery at higher descent rates. In previously conducted experiments of rotors operating in the VRS, the local thrust minimum was generally found at approximately $v_z/v_h \approx -1.2$, which corresponds to $v_z = -6\,\mathrm{m/s}$ for the experiments. Consequently, a similar thrust recovery is expected in the experiments beyond this velocity. This comparison shows that, even though near-identical configurations were investigated in both studies, the computational study predicts reduced thrust losses and a significantly lower critical descent rate ratio. It appears that the experimental data aligns better with previous experiments of rotor performance in axial descent, while the thrust minimum
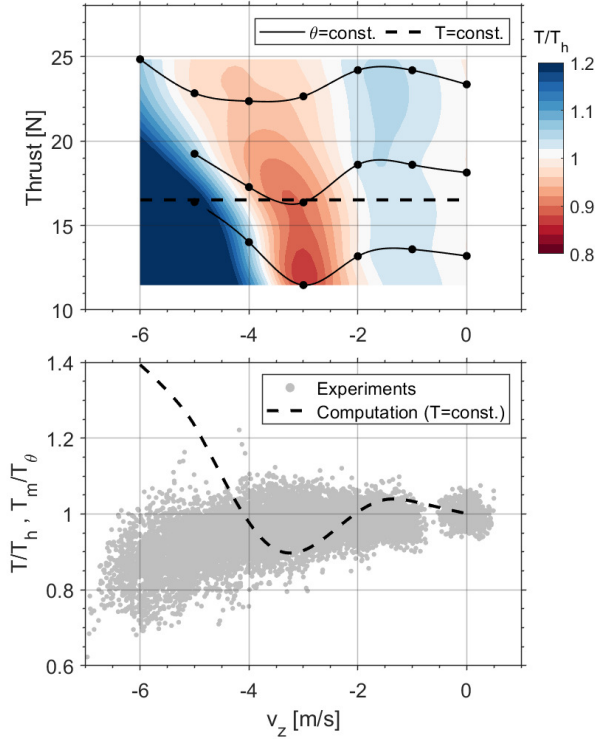
Figure 12. Interpolation of the relative thrust loss for the MAD quadrotor as a function of descent rate, v_z, and thrust using the discrete data points (top), and comparison to experimental results using inferred curve for $T = mg = const$. (bottom).

is predicted at far lower velocities by the computational data compared to those reported in literature.

Sources for Data Discrepancy

Discrepancies between the experimental and computational data were observed, even though near-identical conditions were investigated. Potential systematic errors of both studies, which could amount to these inconsistencies, are addressed and discussed in the following.

Generally, a key difference were the simplifications and assumptions made for the rotor and fuselage geometry in RotCFD. The simulated rotor geometry was similar to the testing rotor geometry (see Fig. 4), but some of the differences could have resulted in some of the observed discrepancies. The simulated rotor was assumed to have a NACA0012 airfoil, which is similar but different from the rotor used in testing. Additionally, the simulated rotor geometry closer to the hub mounting face was modeled as the same chord length as cross section A-A. This should not have resulted in a significant increase in thrust, seeing as the rotor produces significantly less thrust as you get closer to the hub, but it could have contributed to the error. The fuselage CAD model was also simplified prior to implementing it into the simulation domain (covering holes and smoothing edges) so that the grid could more easily render the body of the fuselage. However,

the fuselage was still fairly detailed in the simulation since a very fine grid was used around the body.

Potential oversights in the experimental efforts may have been (1) excessive craft movements despite intended stationary hover (2) excessive attitude fluctuation resulting in misalignment of the thrust vector and gravity vector. Even though the quadrotor was intended to hover stationary over the wind tunnel freestream, it experienced both lateral as well as vertical motion due to reduced controllability. It is well established that the horizontal velocity, along with the vertical velocity, is a primary factor determining the flow state in VRS (Ref. 9). In fact, additional horizontal flow velocities have been shown to increase the maximum thrust loss of a rotor compared to axial conditions. While lateral movements were relatively small and generally less than $0.2\,\mathrm{m/s}$ during experiments, they could have potentially caused minor changes to the overall VRS performance. Additionally, while any vertical craft motion was accounted by adding it to the wind tunnel velocity, it is unclear if this additional vertical motion could impact the formation of the vortex ring system since the descent condition can no longer be considered fully steady. Lastly, while the craft was commanded to stay perfectly level by the flight controller, large vehicle attitude oscillations were recorded during experiments most likely caused by strong fluctuations in the individual rotor thrust. As a consequence, the thrust vector and the gravity vector become misaligned, causing a loss of lift, even though the same thrust is applied. As seen in Fig. 7, vehicle roll and pitch angles of up to $10°$ were recorded, resulting in a loss in lift of $\cos(10°) = 0.985$. Note that the mean angle between the gravity and thrust vector during the flight test in simulated descent was smaller at approximately $\arccos\left(\cos(\overline{\Phi})\cos(\overline{\Theta})\right) = 6\,\mathrm{deg}$, which corresponds to a only relatively small mean loss in lift of $\cos(6°) = 0.995$ for a given thrust. Though, similarly to the vehicle translation, the excessive vehicle rotation could affect the formation of the vortex system and, therefore, change the VRS characteristics.

Similarly, potential sources of systematic errors in the computational approach were be outlined and explored in greater depth: (1) insufficient size of the computational domain, (2) increased levels of turbulence for the quadrotor due to additional rotor-rotor interactions, resulting in longer convergence times, or (3) inadequate gridding. With a size of $14\,\mathrm{m} \times 14\,\mathrm{m} \times 21\,\mathrm{m}$ the computational domain was chosen significantly larger than the investigated quadrotor and boundary effects were assumed to be negligible. This was confirmed by the flow field analysis where the local rotorcraft flow field was fully contained within the center of the domain. Furthermore, it was examined if increased level of turbulence in the VRS could lead to longer convergence times of the aerodynamic coefficients, and if computational length potentially did not account for this. To investigate the convergence properties of the solution, selected computations were performed with double the amount of time steps, yielding only marginal differences. Computations were also performed with varying levels of grid refinement, yielding only marginal differences. However, RotCFD has limitations and can not run on a regular workstation with more than about 2 million cells.

In sum, none of the above mentioned scenarios could be shown to amount the discrepancies between experiments and computations and the exact reasons are still unclear. More data from both studies is needed to identify the source of error with certainty.

Rotor-Rotor and Rotor-Body Interactions

A comparative study involving four rotors and a single rotor, both without the vehicle fuselage, was performed and compared to the computational results of the Stingray model (four rotors with vehicle fuselage) to identify rotor-interactional effects and fuselage-interference in descent. All cases utilized the same rotor geometry and rotor operational parameters, with $\theta = 10°$ and $v_{tip} = 94.6\,\text{m/s}$. For comparison, the mean rotor thrust of all three cases (averaged over all rotors for the 4 rotor configurations) as a function of descent velocity is shown in Fig. 13. Note here, that the trend lines were inferred from a limited number of data points as a preliminary investigation and should be treated with caution.

At hover and low descent rates the thrust values are nearly identical (referring to the blue and red line for these values), however they start to diverge at descent rates of $v_z = -3\,\text{m/s}$ and higher. While all configurations similarly display the characteristic thrust minimum, the influence of multiple rotors and of the fuselage appears to be profound, both of which shift the critical descent rate towards lower velocities and simultaneously reduce the maximum extent of the thrust losses. Specifically, the thrust of the Stingray reaches the lowest point at $v_z = -3\,\text{m/s}$, after which it recovers, exceeding the hover thrust at $v_z = -5\,\text{m/s}$. Meanwhile, the single rotor minimum thrust occurs at considerably higher velocities of around $v_z = -5\,\text{m/s}$ and increases subsequently. Thus, it appears that, while all cases exhibit the same general trends, these configurations are not equivalent in the computational environment when regarding the axial descent performance. These findings are surprising, since a closer agreement between the investi-
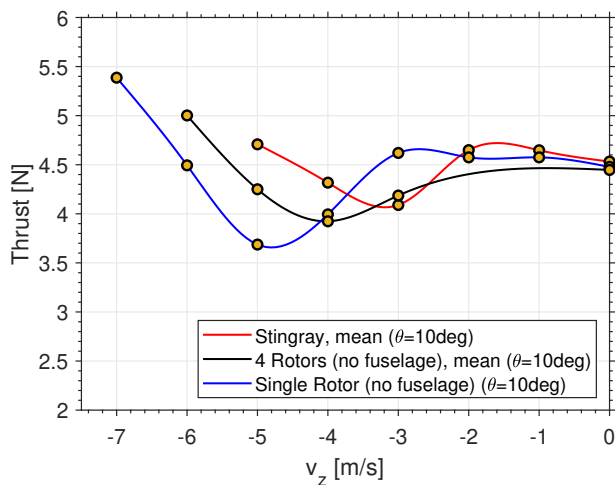
gated cases with less influence of rotor-rotor interactions and fuselage interference was expected.

Radial Blade Loading in Descent

The radial blade loading of the single rotor configuration without fuselage was analyzed in RotCFD for different descent velocities to identify the region of the blade where the majority of thrust losses occur. Figure 14 plots the radial variations of the thrust coefficient for selected descent speeds, where the total thrust of the rotor is given by:

$$T = N_b\rho A(\Omega R)^2 \int_0^1 \frac{dC_T}{dr}dr = N_b\rho A(\Omega R)^2 \int_{r_c}^1 \frac{dC_T}{dr}dr. \quad (27)$$

Note that the rotor blades in RotCFD were modeled with a root cutout of $r_c = 0.225$ and the blade thrust is zero for $r < r_c$. The single rotor configuration was selected in this case to avoid rotor-rotor interactions and potentially varying blade loading distribution throughout the revolution of the rotor. Results indicate, that the small thrust gains at low descent rates ($v_z = -3\,\text{m/s}$) stem from a higher local blade loading near the rotor tip, while the loading on the inboard region is nearly identical to hover conditions. At $v_z = -5\,\text{m/s}$, where the thrust losses are most pronounced for the single rotor (compare with Fig. 13), the majority of thrust losses are found to occur close to the tip, for $r > 0.7$, while the inboard region of the blade is only showing minor differences compared to the hover performance. Meanwhile, at $v_z = -7\,\text{m/s}$ thrust increases uniformly from the VRS conditions as the rotor enters the turbulent wake state, but the thrust gradient at the tip is still less than at hover.

These results indicate that the performance losses of a rotor in the VRS are a localized effect, predominantly occurring in the near-tip region at $r > 0.7$. This effect is assumed to be caused by blade-vortex interactions at the rotor tip, due to the fact that rotor tip vortices are no longer transported away from the rotor disk in axial descent, but instead they accumulate within the rotor plane. These strong blade-vortex interactions are believed to cause local inflow variations leading to reduced local thrust coefficients.
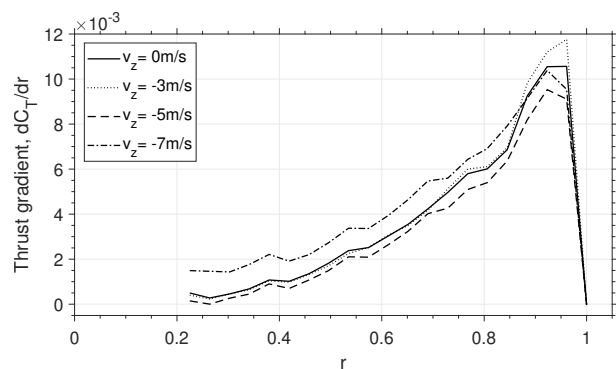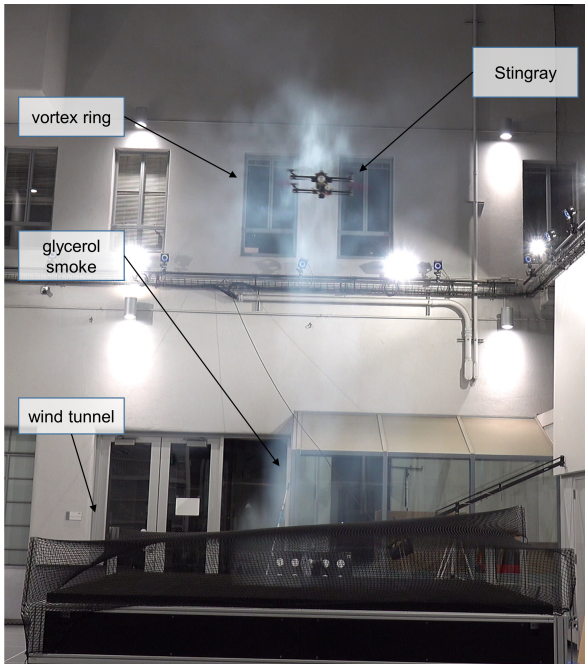

Figure 13. Comparison between computational results of a single rotor and quadrotor (both without the body), all at $\theta = 10°$.

Figure 14. Radial variation of the blade thrust coefficient for selected descent rates.
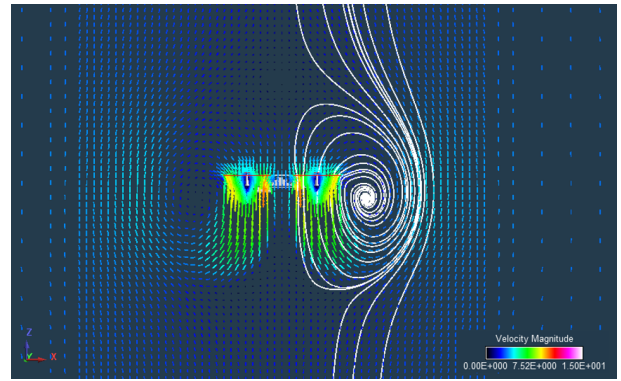
FLOW FIELD ANALYSIS

Visualization of the flow field around the Stingray during the experimental runs was attempted using glycerol smoke, which was injected into the wind tunnel freestream flow, upstream of the wind tunnel. In practice, it proved generally challenging to capture the complete rotor flow field using this visualization technique as smoke was heavily dispersed by the wind tunnel, and most of the smoke was redirected by the rotor flow to pass around the rotorcraft without being ingested through the rotor. Figure 15 shows a selected snapshot at a simulated descent velocity of approximately 3.5 m/s, in which the vortex ring system forming around the front-left rotor appears to have been captured. The smoke, which passed through the rotor and is subsequently re-directed by the external freestream, faintly outlines a ring-like flow path. The core of this vortex ring appears to be in, or very close to the rotor plane, which is in qualitative agreement with the analogous computational results using the same vehicle configuration and rotor platform, shown in Fig. 16. Here, the computational vector field and overlayed streamlines, obtained at the descent velocity where the rotor system experienced the most significant aerodynamic losses, clearly reveal the toroidal vortex ring system, with a vortex core close to the rotor plane.

The vector fields of a single rotor without fuselage shown in Fig. 17 similarly feature this characteristic vortex ring system around the disk. The vortex ring starts to clearly form at descent rates of $v_z = -4$ m/s ($v_z/v_h = -0.75$) and higher, coinciding with the velocities, where the single rotor experienced reduced thrust compared to hover conditions ($T/T_h < 1$, compare to Fig. 13). Furthermore, the vortex core shifts upwards with increasing descent rate and is again found very close to the rotor plane at the same descent velocity, where the most

(a) Streamlines outlining the vortex ring system
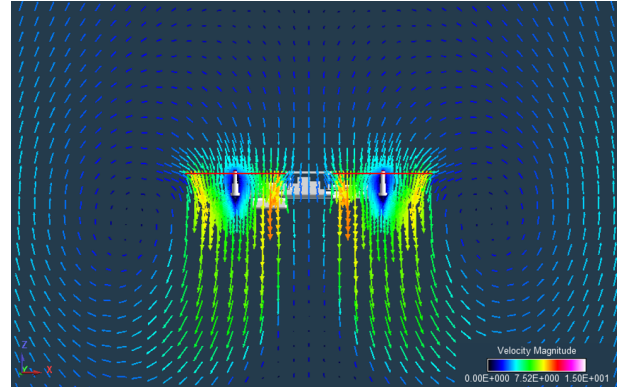
(b) Zoomed in vector field

Figure 16. Vector field of the Stingray at $v_z = -3$ m/s, $v_z/v_h = -0.56$ around the front two rotors.
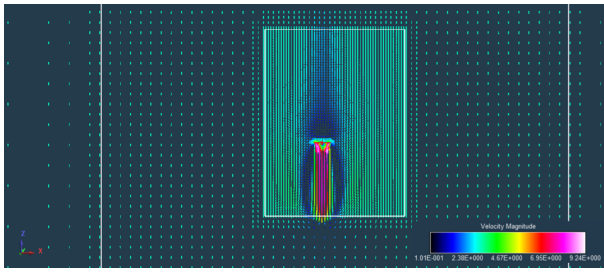
significant thrust losses occur.

One interesting qualitative distinction between the flow field of the single rotor and the Stingray with four rotors in the VRS is that no clearly defined vortex rings is observable between the individual rotors of the Stingray. This suggests that the individual toroidal vortex rings of each rotor merge to form a much larger continuous vortex ring system around the vehicle. Since the grid was heavily refined near the rotors, it is assumed here that this observation is not an artifact of the gridding of the domain, where an insufficiently refined grid may not be able to pick up this vortex structure in between rotors.
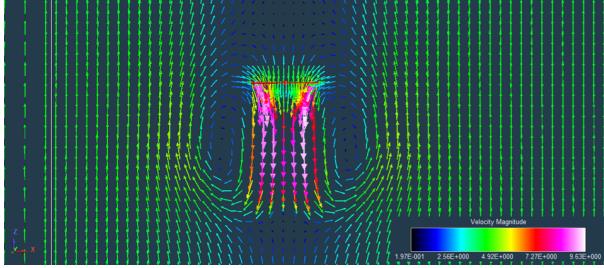
FUTURE WORK

Findings and Recommendations for MAD in Upcoming Mars Missions

Contingent on the success of the currently operated Ingenuity system of the Mars 2020 mission, future exploration of the Martian surface will likely progress towards utilizing dedicated science rotorcraft, which can cover significantly larger distances than a comparable ground-based vehicle. This study sought to evaluate the feasibility of an aerial deployment of this dedicated science rotorcraft during the atmospheric EDL process. Results have shown that the adverse rotor aerodynamics during the VRS can significantly impair the thrust generation with maximum thrust losses of up to 20% compared
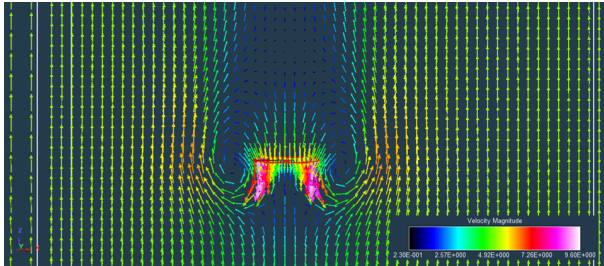

Figure 15. Flow visualisation during an experimental run using glycerol smoke ($v_z \approx -3.5$ m/s, $v_z/v_h \approx -0.67$).

(a) $v_z = -3\,\mathrm{m/s}$, $v_z/v_h = -0.56$

(b) $v_z = -4\,\mathrm{m/s}$, $v_z/v_h = -0.75$

(c) $v_z = -5\,\mathrm{m/s}$, $v_z/v_h = -0.94$

Figure 17. Vector field of a single rotor at different descent velocities.

to hover conditions. Furthermore, these thrust losses are accompanied by strong rotor thrust fluctuations, inducing severe roll and pitch oscillations of the vehicle and limiting stability and controllability. Consequently, any future rotorcraft specifically designed for Mars MAD has to be sufficiently margined in terms of overall thrust capability as well as control authority to minimize the risk level of mission failure after rotorcraft release. More importantly, certain adaptations to the deployment sequence and attempts to completely avoid VRS conditions during MAD could further help to reduce the risks associated with this novel EDL technique. Regardless, the MAD concepts offer many advantages over traditional landing means and should be explored in greater depth.

Noteworthy is that the presented findings largely followed the well-established trends for VRS, which can provide a first-order estimate for the design of a suitable vehicle and the MAD sequence. Given appreciable differences between experiments and computation, any future computational study of MAD scenarios should ultimately be validated against experiments performed under equivalent conditions (i.e., in environmental chambers) when possible and against analogous Earth-relevant experiments when not possible. This will become particularly important if the Mars science rotorcraft will utilize multiple rotors and/or feature a large fuselage planform

area compared to the overall rotor disk area since the cases including a fuselage and multiple rotors resulted in the greatest discrepancies between experimental and RotCFD data.

Limitations and Future Objectives

While this study provided valuable findings regarding the axial descent of variable-pitch multirotors, in particular, the thrust loss due to the adverse VRS aerodynamics, certain shortcomings were noted, which could be improved upon in subsequent investigations. One such shortcoming of the experimental approach was the fact that test flights were performed under manual pilot control. This prevented the investigation of higher descent rates beyond $6\,\mathrm{m/s}$, due to reduced controllability. Thus, a key objective for future and more sophisticated studies is the implementation of an autonomous onboard controller to execute feedback setpoint control over the wind tunnel for a more stable hover flight in the vertical freestream with significantly improved position accuracy. This will allow the examination of higher descent rates, spanning the entire critical axial descent regime from $-2v_h < v_z < 0$, while also reducing vehicle movement over the wind tunnel to provide more accurate aerodynamic data. Apart from this, supplementary fixed-mounted tests of the rotorcraft are anticipated in the future, which can help to remove the constraints imposed by the free-flight experimentation (e.g. thrust matching to the vehicle weight is no longer necessary and collective pitch angles can remain constant throughout a test run). This will allow a greater variety in the investigated scenarios and enables direct comparisons between computations and experiments to identify the current sources for discrepancies. Nonetheless, a continuation of the free-flight tests is anticipated in future, to fully capture the vehicle dynamics in the VRS.

Future RotCFD efforts are expected to focus on improving the fidelity of the simulations by continuing to investigate the effects of fuselage influence and rotor-to-rotor interactions on the rotor performance and flow field. Subsequently, analogous axial descent studies under Mars relevant conditions can be performed. Overall, as future Mars rotorcraft designs become more concrete, experiments as well as computations should incorporate the exact geometric design and should also aim for dynamic similarity between the tests and Mars conditions. Furthermore, the inflow blocking and other aerodynamic interferences by the backshell are critical during the rotorcraft release. Initial RotCFD studies have already been published on this topic (Ref. 3) and experimental efforts are ongoing, using a scaled backshell model over the vertical wind tunnel.

CONCLUSIONS

Experimental and computational efforts have been carried out in parallel, investigating the axial descent performance of a variable-pitch multirotor. The results of this study are anticipated to inform the mid-air-release of future Mars rotorcraft from an entry capsule backshell, evaluating the feasibility to first-order and identifying critical fields of research for more

focused investigations. The key findings presented throughout the paper are as follows:

1. Experimental approach:

   (a) two methods were utilized for estimating the in-flight forces, one based on IMU accelerations and a separate one based on PWM signals sent to the servos for controlling the rotor pitch. Adopting two independent thrust estimators allowed to quantify the relative thrust loss in simulated descent compared to hover conditions without rigid attachment to a load cell.

   (b) increasing mean thrust losses with increasing descent rate were observed during flights in a vertical wind tunnel freestream. Peak losses, recorded at the highest descent rate of $v_z = -6\,\mathrm{m/s}$ were up to 20%.

   (c) rotor thrust fluctuations as well as roll and pitch oscillations were shown to increase drastically with descent rate.

   (d) the induced velocity of the rotor system was calculated and compared to established models of the VRS, indicating an overall good agreement. This suggests that established VRS models apply to these multirotor configurations as well.

2. Computational approach:

   (a) the rotor performance at three discrete pitch angles ($\theta = 8°, 10°$, and $12°$) was analyzed in RotCFD for various descent velocities. Results showed thrust losses of up to 15%.

   (b) the maximum extent of mean thrust losses appeared to decrease when increasing pitch, while the critical descent rate ratio, where maximum losses occur, remained unchanged at $v_z/v_h = -0.65$ for all pitch angles.

   (c) a comparison between the experimental and computational results showed similar thrust losses for both studies, however the critical descent rate ratio was found to be significantly lower in the computations

   (d) a comparison study of a single rotor and four rotors, both without fuselage, indicated considerable differences in the trends of thrust relative to the hover thrust vs. descent rate, suggesting substantial fuselage interference and rotor-rotor interactions in axial descent.

   (e) flow field analysis helped to visualize the toroidal vortex ring system characteristic for axial descent of rotorcraft. This vortex ring system could be observed in experiments as well as in the computations. The computational flow fields showed that once the vortex ring starts to become clearly defined, thrust losses start to manifest themselves. The core of this vortex system shifts upwards and closer to the rotor disk as descent rate increases. At the critical descent rate, where the thrust generation is most compromised, the vortex core is near the rotor plane. At higher descent rates, it shifts above the rotor.

   (f) analysis of the radial rotor blade loading suggests that the majority of thrust loss occurs near the rotor tip ($r > 0.7$), which can be explained by blade-vortex-interactions in this region.

ACKNOWLEDGMENTS

REFERENCES

1. Grip, H. F., Johnson, W., Malpica, C., Scharf, D., Mandic, M., Young, L. A., Allan, B., Mettler, B., and San Martin, M., "Flight Dynamics of a Mars Helicopter," , 2017.

2. Balaram, B., Canham, T., Duncan, C., Grip, H. F., Johnson, W., Maki, J., Quon, A., Stern, R., and Zhu, D., "Mars Helicopter Technology Demonstrator," *AIAA Atmospheric Flight Mechanics Conference*, 2018.

3. Young, L. A., Delaune, J., Johnson, W., Withrow-Maser, S., Cummings, H., Sklyanskiy, E., Izraelevitz, J., Aaron Schutte, A. F., and Bhagwat, R., "Design Considerations for a Mars Highland Helicopter," , Nov 2020.

4. Withrow, S., Johnson, W., Young, L. A., Cummings, H., Balaram, J., and Tzanetos, T., "An Advanced Mars Helicopter Design," *ASCEND 2020*, 2020, p. 4028.

5. Cutler, M., Ure, N., Michini, B., and How, J., "Comparison of Fixed and Variable Pitch Actuators for Agile Quadrotors," , 08 2011. DOI: 10.2514/6.2011-6406

6. Lorenz, R. D., Turtle, E. P., Barnes, J. W., Trainer, M. G., Adams, D. S., Hibbard, K. E., Sheldon, C. Z., Zacny, K., Peplowski, P. N., Lawrence, D. J., *et al.*, "Dragonfly: A Rotorcraft Lander Concept for Scientific Exploration at Titan," *Johns Hopkins APL Technical Digest*, Vol. 34, (3), 2018, pp. 14.

7. Rapin, W., Fraeman, A., Ehlmann, B., Mittelholz, A., Langlais, B., Lillis, R., Sautter, V., Baratoux, D., Payré, V., Udry, A., Horgan, B., Flahaut, J., Dromart, G., Quantin-Nataf, C., Mangold, N., Maurice, S., Keane, J., and Bapst, J., "Critical Knowledge Gaps in the Martian Geological Record: A Rationale for Regional-Scale in situ Exploration by Rotorcraft Mid-Air Deployment," *White paper for the NASEM Planetary Science Decadal Survey*, 2020.

8. Delaune, J., Izraelevitz, J., Young, L. A., Rapin, W., Sklyanskiy, E., Johnson, W., Schutte, A., Fraeman, A., Scott, V., Leake, C., Ballesteros, E., Withrow, S., Bhagwat, R., Cummings, H., Aaron, K., Veismann, M., Wei, S., Lee, R., Madrid, L. P., Gharib, M., and Burdick, J., "Motivations and Preliminary Design for Mid-Air Deployment of a Science Rotorcraft on Mars," , 2020.

9. Johnson, W., "Model for Vortex Ring State Influence on Rotorcraft Flight Dynamics," Technical Report NASA/TP-2005-213477, NASA, 12 2005.

10. Shetty, O., and Selig, M., "Small-scale propellers operating in the vortex ring state," 49th AIAA Aerospace Sciences Meeting including the New Horizons Forum and Aerospace Exposition, 2011.

11. Stack, J., Caradonna, F. X., and Savaş, Ö., "Flow visualizations and extended thrust time histories of rotor vortex wakes in descent," *Journal of the American Helicopter Society*, Vol. 50, (3), 2005, pp. 279–288.

12. Betzina, M. D., "Tiltrotor Descent Aerodynamics: A Small-Scale Experimental Investigation of Vortex Ring State," *American Helicopter Society 57th Annual Forum, Washington, DC*, 2001.

13. Langkamp, D., and Crowther, W., "The role of collective pitch in multi rotor UAV aerodynamics," , 2010.

14. Rajagopalan, R. G., Baskaran, V., Hollingsworth, A., Lestari, A., Garrick, D., Solis, E., and Hagerty, B., "RotCFD-A Tool for Aerodynamic Interference of Rotors: Validation and Capabilities," *Future Vertical Lift Aircraft Design Conference, San Francisco, CA*, 2012.

15. Leishman, J. G., *Principles of Helicopter Aerodynamics*, Cambridge aerospace series, Cambridge University Press, second edition, 2006.

16. Johnson, W., *Helicopter Theory*, Princeton University Press, Princeton, NJ, 1980.

17. Cutler, M., and How, J. P., "Analysis and Control of a Variable-Pitch Quadrotor for Agile Flight," *Journal of Dynamic Systems, Measurement, and Control*, Vol. 137, (10), 101002, 07 2015. DOI: 10.1115/1.4030676

18. Pretorius, A., and Boje, E., "Design and modelling of a quadrotor helicopter with variable pitch rotors for aggressive manoeuvres," *IFAC Proceedings Volumes*, Vol. 47, (3), 2014, pp. 12208–12213.

19. Koning, W. J., "Wind Tunnel Interference Effects on Tilt Rotor Testing using Computational Fluid Dynamics," *NASA/CR—2016–219086*, 2016.

20. Conley, S., Russell, C., Kallstrom, K., Koning, W., and Romander, E., "Comparing RotCFD Predictions of the Multirotor Test Bed with Experimental Results," *Vertical Flight Society's 76th Annual Forum & Technology Display, Virtual*, 2020.

21. Perez, B. P., Ament, G. A., and Koning, W. J., "Experimental Forward Flight Rotor Performance Testing From Terrestrial to Martian Atmospheric Densities," *Moffett Field, California, NASA/CR–2019–220229*, 2019.

22. Perez, B. N., "Forward Flight Rotor Performance at Martian Atmospheric Densities and Sensitivity to Low Reynolds Numbers," *VFS Aeromechanics for Advanced Vertical Flight Technical Meeting*, 2020.